Virtual process chain of sheet molding compound: development, validation and perspectives

Johannes Görthofer, Nils Meyer, Tarkes Dora Pallicity, Ludwig Schöttl, Anna Trauth, Malte Schemmann, Martin Hohberg, Pascal Pinter, Peter Elsner, Frank Henning, Andrew Hrymak, Thomas Seelig, Kay A. Weidenmann, Luise Kärger, Thomas Böhlke

Angaben zur Veröffentlichung / Publication details:

Görthofer, Johannes, Nils Meyer, Tarkes Dora Pallicity, Ludwig Schöttl, Anna Trauth, Malte Schemmann, Martin Hohberg, et al. 2019. "Virtual process chain of sheet molding compound: development, validation and perspectives." *Composites Part B: Engineering* 169: 133–47. https://doi.org/10.1016/j.compositesb.2019.04.001.

Virtual process chain of sheet molding compound: Development, validation and perspectives

Johannes Görthofer[a], Nils Meyer[b], Tarkes Dora Pallicity[a], Ludwig Schöttl[c], Anna Trauth[c], Malte Schemmann[a], Martin Hohberg[b,g], Pascal Pinter[c], Peter Elsner[c,d], Frank Henning[b,d], Andrew Hrymak[e], Thomas Seelig[f], Kay Weidenmann[c], Luise Kärger[b], Thomas Böhlke[a,*]

[a] Institute of Engineering Mechanics, Karlsruhe Institute of Technology (KIT), Germany
[b] Institute of Vehicle System Technology, Karlsruhe Institute of Technology (KIT), Germany
[c] Institute for Applied Materials - Materials Science and Engineering, Karlsruhe Institute of Technology (KIT), Germany
[d] Fraunhofer Institute for Chemical Technology, Pfinztal, Germany
[e] Department of Chemical and Biochemical Engineering, Western University (UWO), London, Canada
[f] Institute of Mechanics, Department of Civil Engineering, Geo and Environmental Sciences, Karlsruhe Institute of Technology (KIT), Germany
[g] SIMUTENCE, Virtual Composite Solutions, Karlsruhe, Germany

A B S T R A C T

A virtual process chain for sheet molding compound (SMC) composites is established and validated by means of experimental investigations on a demonstrator structure. The flow in the compression molding step is simulated via a Coupled-Eulerian-Lagrangian approach using an anisotropic non-Newtonian fluid flow model. Evolution of the fiber orientation distribution (FOD) is described by Jeffery's equation. The predicted FOD is mapped to structural simulations employing a neutral data format. A mean-field anisotropic damage model is used to predict the damage evolution in the demonstrator. Simulated FOD at the end of the compression molding is validated by computer tomography. Structural simulations are validated by means of a cyclic four-point bending test on the demonstrator. The predicted results show increased accuracy with the experiments by transferring FOD data within the virtual process chain. Critical points of high damage concentrations leading to failure agree with the experimental observations.

1. Introduction

Fiber reinforced polymers stand out due to their high specific stiffness and strength. An important advantage of chopped discontinuous fiber reinforced polymers are low material and manufacturing costs and the high freedom of design. Therefore, parts with complex geometries and integrated ribs, beads etc. can be manufactured. Among this type of composites, sheet molding compound (SMC) has become a very attractive material especially for exterior parts in the automotive industry [1,2]. SMC consists of a thermoset resin reinforced with chopped fibers and eventually some amount of fillers. SMC parts are produced within a compression molding process. Compared to injection molding, compression molding convinces with an enhanced strength and toughness of the final part due to longer fibers [3].

With an eye towards the developments within Industry 4.0, an established and functional virtual process chain is a powerful tool. The digital twin of the production process is suitable and flexible for, e.g., development and testing of new components, optimization of manufacturing processes or adjustment of components to change in boundary conditions. Already for some time, virtual process chains, including material modeling and process simulation, have proven to reduce the cost and time of product development processes by predicting the structural behavior in good agreement with reality. Commercial software linking tools such as FEDES [4] and MPCCI [5,6] are available for metal processing and its structural simulation.

The effects of process simulation results on structural simulations are even more distinct for fiber reinforced polymers due to re-orientation of fibers during the manufacturing process. Such coupling has already been considered in short fiber thermoplastic injection molding with a validation employing a demonstrator [7] and they are commercially available in DIGIMAT and Converse for this field of application. For continuous fiber reinforced polymers, the holistic simulation is still under development. Within this material class, the virtual process

* Corresponding author. Kaiserstraße 10, 76131, Karlsruhe, Germany.
E-mail address: thomas.boehlke@kit.edu (T. Böhlke).

chain for Resin Transfer Molding (RTM) shows the highest level of development [8–10]. For the compression molding process of long fiber reinforced thermoplastics, Buck et al. [11] showed the effect of coupling the process and structural simulation. Initial approaches of a holistic virtual process chain for SMC compression molding are presented by Hohberg et al. [12].

Like for most discontinuous fiber reinforced materials, the mechanical behavior of an SMC component depends on the fiber orientation distribution, which is sensitive to, e.g., changes in initial charge position and manufacturing process conditions. Therefore, it is necessary to simulate the compression molding process as it results in a process-dependent macro-heterogeneous anisotropic fiber orientation distribution. Based on the microstructure, micromechanical homogenization allows for a prediction of the resulting macroscopical mechanical behavior. Hereby, a profound understanding of the physical material behavior and the determination of the required material parameters via corresponding characterization techniques is crucial. Furthermore, in order to validate the process and structural simulations, experimental techniques by means of microstructure analysis and mechanical testing are desirable.

Generally, a virtual process chain of SMC comprises two major steps: compression molding simulation and structural simulation. A short overview on the state of research of material modeling in each step is described subsequently. In case of compression molding simulations, on one hand approaches have been developed that apply two-phase methods based on Darcy's law [13] or separate fiber and matrix speeds with a model transition for different flow regimes [14]. On the other hand, direct fiber simulations [15] enable detailed studies on fiber orientation, e.g., at rib geometries [16,17]. However, the majority of models considers SMC as one-phase medium, which was initially described with generalized Hele-Shaw models [18], utilizing the relatively small thickness of SMC plates compared to their longitudinal dimensions. As pointed out by Castro and Griffith [19], those early generalized Hele-Shaw models do not capture the flow behavior observed in experiments [20]. More accurate models separating a central plug flow and an outer lubrication layer were developed [19,21,22] and extended for the non-Newtonian SMC behavior [23,24]. The compression molding simulation presented in the present work considers SMC a three dimensional, one-phase, weakly compressible [25,26], anisotropic, non-Newtonian material that experiences slip at the molds due to the lubrication layer. The flow is accompanied by re-orientation of fibers, which is modeled by an evolution equation for the second order fiber orientation tensor.

In case of structural simulations, models describing the material behavior of fully cured SMC parts due to external loadings have been developed, in which many take the microstructure into account. Hereby, focus lies on the stiffness degradation due to damage onset on the microscale. Experimental investigations on the stiffness dependency on the temperature and the loading frequency are performed [27]. Furthermore, experimental characterizations that investigate the stiffness degradation of SMC parts (uniaxial and biaxial) are presented [28]. Numerically the stiffness degradation can be captured, e.g., by an equivalent, anisotropic inhomogeneity ansatz for damaged fibers [29]. The fiber-matrix interface traction vector is related to the stress in the inclusion, which is modeled as a linear function of the macroscopic stress using a fourth-order localization tensor [30,31]. Under the assumption of a perfect interface, the traction as well as the displacement vector across the interface are continuous. The normal and shear stress components on a perfect interface are the projections of the traction vector. The equivalent local stress is frequently coupled linearly from the normal and shear stress [32]. Some models use a probabilistic distribution for the interface strength solely [33] or for the strength of all considered phases (matrix, fibers, interfaces) [34]. Another approach is the introduction of a microcrack density parameter which is used to decrease the fiber strain localization [35]. In order to adequately model the behavior within a homogenization framework, models need to be as precise and detailed as possible. Besides, to apply such structural damage models to large calculations of macroscopic components the models need to be efficient and implemented deftly. In the literature, approaches such as a numerical Eshelby tensor [36] or an interface debonding representation based on void nucleation [37,38] are used, for example. The damage model used in this paper takes into account an empirical definition of the fiber orientation distribution based on discrete damage directions [39]. This model can be coupled to compression molding simulation results and can be used within a virtual process chain.

In this paper, a virtual process chain is presented, which couples the compression molding simulation with the structural simulation by transferring fiber orientation information. The virtual process chain is validated by means of a physical process chain using a demonstrator. Section 2 provides an overview of the production process (physical process chain) and the demands for a virtual process chain are described shortly. Section 3 presents the modeling of the two major steps of the virtual process chain, i.e., compression molding simulation and structural simulation. These two steps are connected using mapping procedures for fiber orientation data. Section 4 describes the application to a demonstrator from an experimental as well as a simulative perspective. The fiber orientation distribution is obtained using X-ray computed tomography (CT) scans and the demonstrator is subjected to a four-point bending load. The introduced virtual process chain is applied. All simulated and measured results are compared and discussed in Section 5. The paper finishes with conclusions and future perspectives that are drawn in Section 6.

A direct tensor notation is used throughout the manuscript to describe the equations. All vector and tensor components refer to an orthonormal vector basis $\{\boldsymbol{x}, \boldsymbol{y}, \boldsymbol{z}\}$. Vectors are denoted by lower case bold letters (e.g. $\boldsymbol{a}$), while second order and fourth order tensors are denoted by upper case bold letters (e.g. $\boldsymbol{A}$) and upper case blackboard bold letters (e.g. $\mathbb{A}$), respectively. The composition of 2 s order or fourth order tensors is formulated by $\boldsymbol{AB}$ and $\mathbb{AB}$, respectively. A linear mapping of vectors by second order tensors and second order tensors by a fourth order tensor is written as $\boldsymbol{a} = \boldsymbol{Cb}$ and $\boldsymbol{A} = \mathbb{C}[\boldsymbol{B}]$. The scalar product is denoted by $\boldsymbol{A}\cdot\boldsymbol{B}$ and $\mathbb{A}\cdot\mathbb{B}$. The Frobenius norm of a second order tensor is defined as $\boldsymbol{A} = \sqrt{\boldsymbol{A}\cdot\boldsymbol{A}}$. The gradient of a vector field $\boldsymbol{a}$ and the divergence of a second order tensor field $\boldsymbol{A}$ are defined as

$$\operatorname{grad}(\boldsymbol{a}) \hat{=} \begin{pmatrix} \frac{\partial a_x}{\partial x} & \frac{\partial a_x}{\partial y} & \frac{\partial a_x}{\partial z} \\ \frac{\partial a_y}{\partial x} & \frac{\partial a_y}{\partial y} & \frac{\partial a_y}{\partial z} \\ \frac{\partial a_z}{\partial x} & \frac{\partial a_z}{\partial y} & \frac{\partial a_z}{\partial z} \end{pmatrix}, \qquad \operatorname{div}(\boldsymbol{A}) \hat{=} \begin{pmatrix} \frac{\partial A_{xx}}{\partial x} + \frac{\partial A_{xy}}{\partial y} + \frac{\partial A_{xz}}{\partial z} \\ \frac{\partial A_{yx}}{\partial x} + \frac{\partial A_{yy}}{\partial y} + \frac{\partial A_{yz}}{\partial z} \\ \frac{\partial A_{zx}}{\partial x} + \frac{\partial A_{zy}}{\partial y} + \frac{\partial A_{zz}}{\partial z} \end{pmatrix}.$$

2. Physical process chain and demands for a virtual process chain

2.1. Physical process chain

An overview of the most important key steps within the physical process chain of a compression molded SMC part is presented in Fig. 1. SMC sheets are produced in a pre-production process. After a certain maturing time, these sheets are cut into the required shapes and stacked to form the initial charge for compression molding of an SMC part. The initial charge is placed into a heated mold that is mounted to a press. Subsequently, the mold is closed displacement controlled until a maximum force is reached and the press switches to force controlled consolidation. During the compression step, the SMC begins to flow until the cavity is filled, followed by curing of the matrix. The molded part is then taken out of the press and allowed to cool down to room temperature for secondary machining processes. The final SMC part can then be used for experimental testing for various loading cases and fiber orientation analyses.

2.2. Virtual process chain

Fig. 1 (lower half) shows the key steps of the virtual process chain covering the physical process chain. In order to appropriately simulate the production process, initial conditions (e.g., SMC material data, cavity and initial charge dimensions) need to be known. Further input, such as boundary conditions for the compression molding simulation are taken directly from the corresponding physical step. The compression molding simulation can then be carried out based on an appropriate material model and discretization. In this work, for simplification, residual stress developed in the SMC part due to curing is assumed to be negligible. The structural simulation of the virtually manufactured SMC part needs to take the results of the compression molding simulation into account. Therefore, these results are mapped from the compression molding mesh to the structural mesh. An appropriate structural damage model can then predict the mechanical behavior of the SMC part under various conditions and loading scenarios.

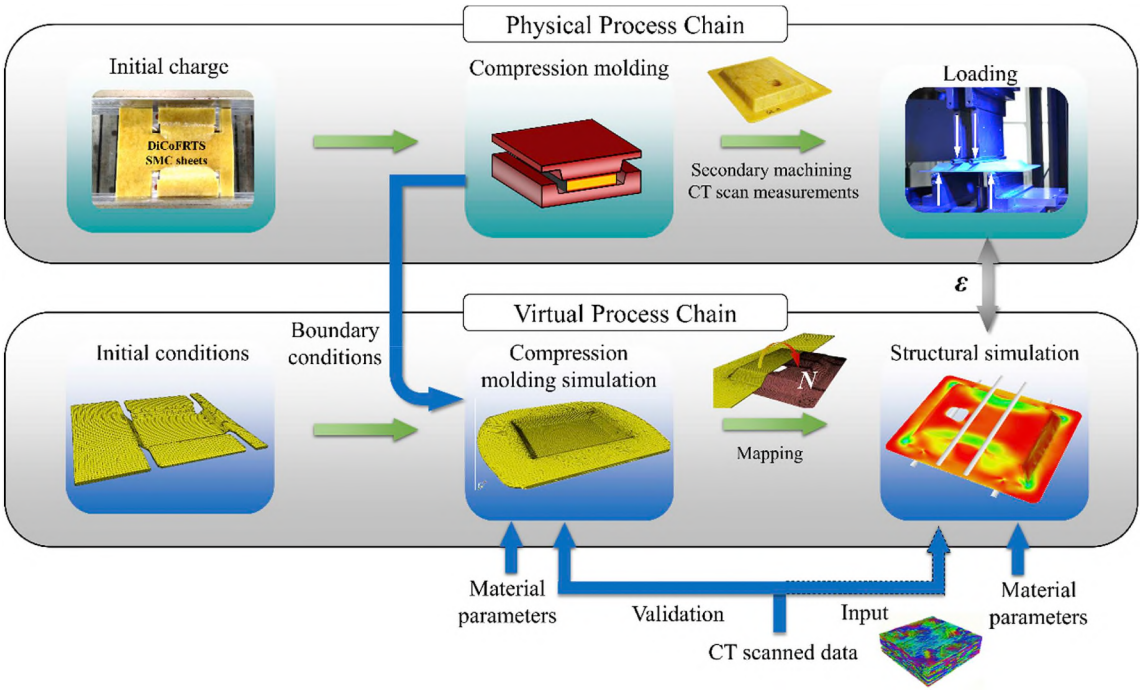

Fig. 1. Physical and virtual process chain steps involved in fabrication of an SMC part.

3. Development of the virtual process chain

3.1. Fiber orientation distribution information

The fiber orientation is the key information that needs to be considered within the virtual process chain. An overview on the utilization of fiber orientation information in the prediction of properties of fiber reinforced polymers is given by Ref. [40]. The fiber orientation information can be depicted as second order fiber orientation tensor $\boldsymbol{N}$, which is defined as

$$\boldsymbol{N} = \oint \boldsymbol{n} \otimes \boldsymbol{n}\, \psi(\boldsymbol{n}) \mathrm{d}n, \tag{1}$$

where $\psi(\boldsymbol{n})$ is the fiber orientation distribution function, $\boldsymbol{n}$ is the fiber direction vector [41] and dn is the surface element on the unit sphere that ensures an invariant integration. The fiber orientation distribution function can be recovered from the tensor according to Refs. [41,42].

Alternatively, the fiber orientation distribution can be expressed in a discrete form as

$$\psi(\boldsymbol{n}) = \sum_{\beta=1}^{K} c(\boldsymbol{n}_\beta)\delta(\boldsymbol{n}, \boldsymbol{n}_\beta), \tag{2}$$

where $\delta(\boldsymbol{n}, \boldsymbol{n}_\beta)$ is the Dirac delta distribution with respect to a specific direction $\boldsymbol{n}_\beta$, $c(\boldsymbol{n}_\beta)$ are the corresponding weights and K is the number of fiber directions. Analogously to Eq. (2), for M fibers with equal length, the fiber orientation tensor $\boldsymbol{N}$ can be empirically expressed as

$$\boldsymbol{N} = \frac{1}{M} \sum_{\gamma=1}^{M} \boldsymbol{n}_\gamma \otimes \boldsymbol{n}_\gamma \tag{3}$$

[41,42]. The fiber orientation information is passed between the steps of compression molding simulation and structural simulation. Additionally, fiber orientation information from CT scans are used as an input to the structural simulation for investigating the effect of deviation in predicted data. Furthermore, the fiber orientation data taken from the CT scans are also used for validation of the compression molding simulation.

3.2. Compression molding simulation

The characteristic SMC flow is formed by a thin, resin-rich lubrication layer at the mold surface, which arises from the temperature gradient between the hot mold surface and the SMC charge at room temperature as well as the low thermal conductivity of the SMC. Within this lubrication layer, a high velocity gradient occurs, which leads to a constant velocity over the thickness in the core region (Fig. 2), which is often referred to as “plug-flow”. The entire compression molding simulation is isothermal, since only this small layer adjacent to the mold is expected to heat up during the short compression time [43]. The governing equations of the 3D compression molding simulation are described in this section, while implementation, meshing and boundary conditions are discussed in Section 4.3.2.

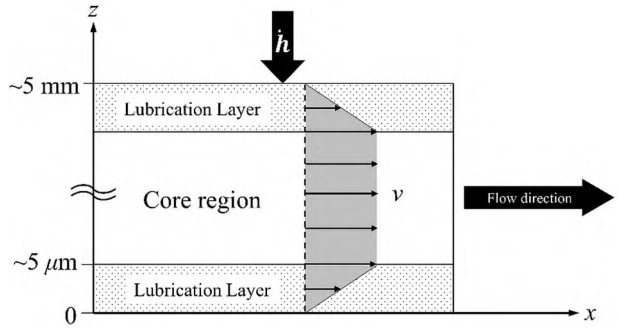

Fig. 2. Schematic cross-section through the SMC plug flow with a lubrication layer and a core region during the compression molding process, and resulting velocity distribution through the thickness [44].

3.2.1. Balance equations

The balance of momentum

$$\rho \frac{\mathrm{D}\boldsymbol{v}}{\mathrm{D}t} = \mathrm{div}(\boldsymbol{\sigma}) \tag{4}$$

is solved using explicit time integration utilizing the ABAQUS Coupled-Eulerian-Lagrangian (CEL) framework, which is based on the work of Benson [45,46]. In Equation (4), $\frac{\mathrm{D}(\cdot)}{\mathrm{D}t} = \frac{\partial(\cdot)}{\partial t} + \mathrm{grad}(\cdot)\boldsymbol{v}$ describes a material derivative, ρ is the mass density and $\boldsymbol{v}$ denotes the velocity vector. The fundamental idea of this approach is to apply an operator split with a Lagrangian step and a subsequent Eulerian transport step. The Eulerian step is calculated by moving the deformed nodes back to their fixed positions and calculating the volume of material transported between neighboring elements [46]. State variables are advected assuming a linear interpolation in each element of the deformed configuration and mapping them to the adjusted configuration based on the volume fractions.

3.2.2. Kinematics

The velocity gradient is computed as

$$\boldsymbol{L} = \frac{\mathrm{D}\boldsymbol{F}}{\mathrm{D}t}\boldsymbol{F}^{-1} \tag{5}$$

using the deformation gradient $\boldsymbol{F}$. The symmetric strain rate tensor and the vorticity tensor are defined as $\boldsymbol{D} = \frac{1}{2}(\boldsymbol{L} + \boldsymbol{L}^{\top})$ and $\boldsymbol{\omega} = \frac{1}{2}(\boldsymbol{L} - \boldsymbol{L}^{\top})$ respectively.

3.2.3. Material modeling

The stress upon deformation is modeled as

$$\boldsymbol{\sigma} = -p\boldsymbol{I} + \boldsymbol{\sigma}'_{\mathrm{rheo}}, \tag{6}$$

where p describes the hydrostatic pressure derived from an equation of state and $\boldsymbol{\sigma}'_{\mathrm{rheo}}$ denotes the deviatoric viscous stress. The equation of state models compressibility of SMC observed in Refs. [26,47] as

$$p = \rho_0 \zeta_0^2 \left(1 - \frac{\rho_0}{\rho}\right) \tag{7}$$

with the compressibility expressed in terms of the speed of sound ζ_0. The relative volume change is expressed utilizing the current mass density ρ and the initial mass density ρ_0.

The viscosity η is calculated using a power-law function suggested by Dumont et al. [24] as

$$\eta = \eta_0 \left(\frac{\boldsymbol{D}'}{D_0}\right)^{n-1}, \tag{8}$$

with a reference deformation rate D_0, power-law coefficient n, reference viscosity η_0 and the deviatoric strain rate tensor $\boldsymbol{D}' = \boldsymbol{D} - \frac{\mathrm{tr}(\boldsymbol{D})}{3}\boldsymbol{I}$. The rheological stress is modeled based on an extension of isotropic viscosity (as discussed in Ref. [48])

$$\boldsymbol{\sigma}'_{\mathrm{rheo}} = 2\eta(\boldsymbol{D}' + \alpha\mathbb{N}[\boldsymbol{D}']), \tag{9}$$

with an empirical coefficient α that couples the viscosity to the fourth order fiber orientation tensor $\mathbb{N}$, that is computed using the invariant based optimal fitting (IBOF) closure [49]. There are multiple fiber orientation models for concentrated suspensions modeling fiber interaction as diffusion process, such as the ARD-RSC model [50]. However, here the diffusion is achieved by modeling anisotropic viscous behavior that naturally causes an increased flow perpendicular to a dominant fiber orientation, similar to the arguments used in Ref. [51]. With the diffusive part covered by the anisotropic flow, the fiber orientation is modeled with Jeffery's equation [52] omitting the need to characterize numerous fitting parameters. Using the vorticity tensor $\boldsymbol{\omega}$ and $\lambda = 1$ for long slender fibers, the tensorial form of Jeffery's equation

$$\frac{\partial \boldsymbol{N}}{\partial t} = \boldsymbol{\omega}\boldsymbol{N} - \boldsymbol{N}\boldsymbol{\omega} + \lambda(\boldsymbol{D}\boldsymbol{N} + \boldsymbol{N}\boldsymbol{D} - 2\mathbb{N}[\boldsymbol{D}]), \tag{10}$$

as proposed by Advani and Tucker [41], is used. The fiber orientation tensor is described with six state variables that are advected according to the description in Section 3.2.1.

The parameters are fitted to experimental results obtained with an extensional flow in-line rheometer [26,47] using the same set of equations reduced to the quasi-1D flow of the rheometer.

The thin hot lubrication layer is modeled as a constant tangential friction stress κ opposing the relative velocity of SMC. This is a simplification considering the results of Barone and Caulk [20] and is applied due to current technical limitations in the implementation of hydrodynamic friction.

3.3. Transfer of fiber orientation distribution information

3.3.1. Mapping from compression molding simulation

Different mesh types are applied throughout the virtual process chain, all of which are highly suitable for their individual application (Fig. 3). However, multiple mapping steps are necessary to transfer data between these meshes. First, the fiber orientation and occupation of cells has to be mapped from the Lagrangian volume mesh, used for forming simulation of the stacked semi-finished sheets, to the Eulerian volume mesh for simulation of the flow. After the compression molding simulation, fiber orientations have to be mapped to the structural shell mesh.

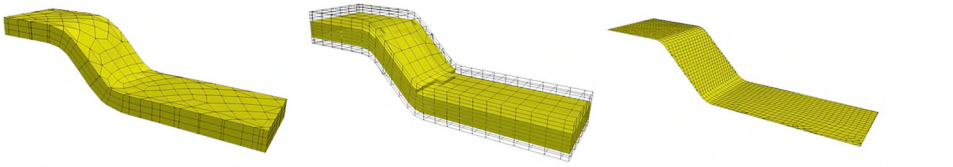

(a) Lagrangian volume mesh (forming) (b) Eulerian volume mesh (molding) (c) Lagrangian shell mesh (damage)

Fig. 3. Lagrangian and Eulerian meshes applied in the virtual process chain.

To facilitate an efficient and software-neutral exchange of information, adapters to the Visualization Toolkit (VTK) file format are created for all applied tools, and the mapping is performed with VTK files. The information to be transferred is defined on elements, thus an element-weighted mapping algorithm of the MPCCI MapLib library is used [6].

3.3.2. Mapping from CT scans

Fiber orientation information obtained by CT scans of real parts is used additionally to the information obtained from the compression molding simulations. On the one hand, this fiber orientation information is used in order to validate the computed results of the compression molding simulation and on the other hand, as an input to the structural simulation. In order to analyze the fiber orientation at a specific point in the scanned part, an orientation tensor $\boldsymbol{N}$ based on Eq. (3) is used to represent the local fiber orientation [53]. In view of a finite element simulation, the fiber orientation is analyzed at the Gaussian points of a structural shell mesh. The analysis is done autonomously for each Gaussian point and is representatively described below on a single Gaussian point. To define the required set of fiber vectors $\boldsymbol{n}_\gamma$, a cylindrical volume B around the Gaussian point is defined. The center axis of the cylinder is aligned along the element normal direction $\boldsymbol{p}$ (shown in Fig. 4).

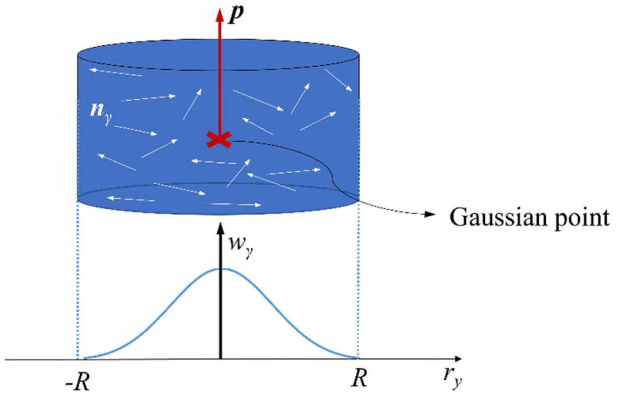

Fig. 4. Cylindrical volume B with evaluation radius R around a Gaussian point and shape of the weighting function w_γ.

The cylinder height is given by the structural mesh shell thickness and the evaluation radius R can be adjusted. In order to give preference to fiber vectors close to the center axis, an additional weighting function w_γ is implemented. Based on all M fiber vectors$\boldsymbol{n}_\gamma$ within the volume B and the additional weighting factorw_γ the second order orientation tensor$\boldsymbol{N}$ is determined by

$$\boldsymbol{N} = \frac{1}{\sum_{\gamma=1}^{M} w_\gamma} \sum_{\gamma=1}^{M} w_\gamma \boldsymbol{n}_\gamma \otimes \boldsymbol{n}_\gamma. \tag{11}$$

The weighting factor w_γ is expressed by the Gaussian function

$$w_\gamma = \exp\left(-\frac{9}{2}\frac{r_\gamma^2}{R^2}\right). \tag{12}$$

This function is distance-based, since r_γ describes the distance of voxel γ to the center axis. The size of the considered local volume B and the shape of the weighting function are coupled and adjusted by R. This evaluation radius R should, on the one hand, be selected sufficiently small so that the resulting orientation tensor $\boldsymbol{N}$ represents the local fiber orientation close to the considered Gaussian point. On the other hand, R should also be large enough to balance imperfection and smooth the resulting tensor field.

3.4. Structural damage modeling of SMC

The process-induced macro-heterogeneous anisotropic microstructure significantly affects the mechanical performance of SMC parts. It is, therefore, necessary to consider the microstructure, obtained by compression molding simulation or microstructure characterization, in the structural simulations. A homogenization approach is used to link the effective macroscopic behavior of the SMC part with its microstructure. In the here presented case, a computationally efficient mean-field homogenization scheme is applied. The micromechanical model accounts for the two dominant damage mechanisms – matrix microcracking and fiber-matrix interface debonding – which lead to an anisotropic evolution of the stiffness. Damage evolution is realized by means of an effective stiffness degradation. The effective stiffness $\bar{\mathbb{C}}$ links the effective strain $\bar{\boldsymbol{\varepsilon}}$ to the effective stress $\bar{\boldsymbol{\sigma}}$ by Hooke's law $\bar{\boldsymbol{\sigma}} = \bar{\mathbb{C}}[\bar{\boldsymbol{\varepsilon}}]$. Hereby, the effective stiffness is approximated by the well-established Mori-Tanaka (MT) [54] homogenization scheme

$$\bar{\mathbb{C}} = \mathbb{C}_\mathrm{M} + c_\mathrm{F}(c_\mathrm{M}\langle(\mathbb{P}_0 + (\mathbb{C}_\mathrm{F} - \mathbb{C}_\mathrm{M})^{-1})^{-1}\rangle_\mathrm{F}^{-1} + c_\mathrm{F}(\mathbb{C}_\mathrm{F} - \mathbb{C}_\mathrm{M})^{-1})^{-1}. \tag{13}$$

Matrix and fiber volume fractions are indicated by c_M and c_F, and $\mathbb{C}_\mathrm{M}$ and $\mathbb{C}_\mathrm{F}$ are the isotropic matrix and fiber stiffness. The orientation average $<\cdot>_\mathrm{F}$ with respect to all fibers can be expressed by means of the discrete fiber orientation distribution as presented in Eq. (2). An explicit expression for Hill's polarization tensor $\mathbb{P}_0$ can be found in Ref. [55]. Interface and matrix damage are modeled by an evolution of $\mathbb{C}_\mathrm{M}$, c_M, c_F and $c(\boldsymbol{n}_\beta)$. Matrix damage depends on the phase-averaged matrix stress $\boldsymbol{\sigma}_\mathrm{M} = \mathbb{B}_\mathrm{M}^{\mathrm{MT}}[\bar{\boldsymbol{\sigma}}]$, obtained by means of the stress localization in the matrix$\mathbb{B}_\mathrm{M}^{\mathrm{MT}}$. The isotropic degradation of the matrix stiffness is expressed as $\mathbb{C}_\mathrm{M} = (1 - d_\mathrm{M})\mathbb{C}_\mathrm{M}^0$. The scalar damage variable $d_\mathrm{M} \in [0,1]$ describes the progression of matrix damage and only depends on the maximum principal phase-averaged matrix stress. The calculation of interface damage is based on the shear $\tau_\mathrm{I}(\boldsymbol{n}_\beta, \boldsymbol{s})$ and normal stress $\{\sigma_\mathrm{I}(\boldsymbol{n}_\beta, \boldsymbol{s})\}$ on the lateral surface of a fiber. A scalar equivalent interface stress $\sigma_{\mathrm{I,eq}}(\boldsymbol{n}_\beta)$ with fiber direction $\boldsymbol{n}_\beta$ is defined according to Ref. [39] as

$$\sigma_{\mathrm{I,eq}}(\boldsymbol{n}_\beta, \boldsymbol{s}) = \hat{\sigma}_{\mathrm{I,eq}}\sqrt[m]{\left(\frac{\tau_\mathrm{I}(\boldsymbol{n}_\beta, \boldsymbol{s})}{\tau_{\mathrm{I}0}}\right)^m + \left(\frac{\{\sigma_\mathrm{I}(\boldsymbol{n}_\beta, \boldsymbol{s})\}}{\sigma_{\mathrm{I}0}}\right)^m}. \tag{14}$$

Hereby, $\{\cdot\}$ is the Macaulay bracket, $\hat{\sigma}_{\mathrm{I,eq}}$, m, $\tau_{\mathrm{I}0}$ and $\sigma_{\mathrm{I}0}$ are parameters and $\boldsymbol{s}$ is the normal vector on the interface. Under the assumption of a Weibull-distributed interface strength in each fiber direction $\boldsymbol{n}_\beta$, a fiber survival probability can be given by

$$P_\mathrm{s}(\boldsymbol{n}_\beta) = \exp\left(-\frac{1}{A_{\mathrm{I}0}}\int_{A_\mathrm{I}}\left\{\frac{\sigma_{\mathrm{I,eq}}(\boldsymbol{n}_\beta) - \sigma_\mathrm{u}}{\sigma_\mathrm{o}}\right\}^k \mathrm{d}A_\mathrm{I}\right) \tag{15}$$

with the four Weibull parameters σ_u, σ_o, k, $A_{\mathrm{I}0}$ and the integral over the lateral fiber surface A_I [56]. Due to experimental findings in the literature, specific parameters are chosen as $m = 2$ and $\frac{\sigma_{\mathrm{I}0}}{\tau_{\mathrm{I}0}} = 1.5$ [32,57,58,59,60]. The remaining parameters can be summarized to three independent parameters and are given in Appendix A.2.

The additive split $c(\boldsymbol{n}_\beta) = \bar{c}(\boldsymbol{n}_\beta) + \check{c}(\boldsymbol{n}_\beta)$ in fibers with intact interfaces $\bar{c}(\boldsymbol{n}_\beta)$ and failed interfaces $\check{c}(\boldsymbol{n}_\beta)$ allows for an estimation of the fraction of fibers with intact interfaces in a direction $\boldsymbol{n}_\beta$. This fraction can be considered the probability $P_\mathrm{I}(\boldsymbol{n}_\beta)$ of finding fibers with intact interfaces in the corresponding direction

$$P_i(\boldsymbol{n}_\beta) = \frac{\bar{c}(\boldsymbol{n}_\beta)}{c(\boldsymbol{n}_\beta)}, \qquad c(\boldsymbol{n}_\beta) > 0. \tag{16}$$

The assumption that the probability $P_i(\boldsymbol{n}_\beta)$ of finding intact fibers can never be higher than the probability $P_s(\boldsymbol{n}_\beta)$ of fibers surviving a given load, leads to the consistency condition $\phi(\boldsymbol{n}_\beta) = P_i(\boldsymbol{n}_\beta) - P_s(\boldsymbol{n}_\beta) \leq 0$. This consistency defines an anisotropic evolution of fibers with failed interfaces and an anisotropic evolution of the overall stiffness, respectively.

The considered mean-field damage model is discussed in more detail in Ref. [39]. The material model is implemented in the ABAQUS/Standard user subroutine UMAT for shell elements in a co-rotational framework [61]. The heterogeneous local fiber orientation distribution is obtained by means of second order fiber orientation tensors from compression molding simulations (see Section 3.3.1) or microstructure characterization (see Section 3.3.2) in each finite element. A subsequent interpolation approximation of the fiber orientation distribution function following Kanatani [42] leads to the weights $c(\boldsymbol{n}_\beta)$, whereas $c(\boldsymbol{n}_\beta) \geq 0$ has to be ensured. As the considered material behavior of SMC is modeled as elastic-damageable (plasticity and viscous effects are negligible), a secant moduli estimation for the effective stiffness $\bar{\mathbb{C}}$ can be used [62,63]. In order to adopt the model to another material class and take, e.g., plasticity into account, the tangent operator will have to be used for the homogenization in the nonlinear regime [64].

4. Application

4.1. Introduction of the demonstrator

A rectangular hollow tray-shaped thin plate (180 mm × 230 mm × 2 mm, details in Appendix A.1) consisting of geometrical feature of curved surfaces and thorough trapezoidal shaped hole is used as a demonstrator to exemplify the virtual process chain of SMC.

Fig. 5(a) shows the geometrical model of the demonstrator with the trapezoidal shaped hole. Dimensional details of the demonstrator are provided in Fig. A1. Fig. 5(b) shows the physical demonstrator manufactured by using the compression molding process at the Fraunhofer Institute for Chemical Technology in Pfinztal. The material for the demonstrator comprises of an unsaturated polyester polyurethane hybrid (UPPH) resin, a new B-stage polymer resin system provided by Aliancys, Schaffhausen, Switzerland and chopped glass fibers (of $d_F \approx 13.5\,\mu m$ in diameter and $l_F \approx 25\,mm$ in length) [26,65]. The measured fiber volume fraction c_F in the demonstrator is 25%.

In the physical process chain of fabricating the demonstrator, initially SMC sheets are compounded in a SMC production line. After the maturing process, the SMC initial charge in the form of rectangular sheets (320 mm × 260 mm) are stacked together to a total thickness of 5.5 mm, which have rectangular slits to improve the preforming of the stack. The volume of this stack is higher than the volume of the demonstrator as the mold cavity is larger than the demonstrator itself (Fig. 10). The initial charge at room temperature conditions (23 °C) is placed into the hot cavity (upper mold at 140 °C and lower mold at 145 °C). Afterwards, the cavity is closed at a constant speed of $\dot{h} = 1\,mm/s$ with a total compression time of 3.5 s by displacement-controlled movement of molds. The control system is then triggered to force control such that the molds apply a constant pressure of 12.5 MPa. The molded part is then taken out of the press and cooled down to room temperature. The demonstrator is cut out from the molded part and the trapezoidal hole is drilled. The demonstrator is tested with a cyclic four-point displacement-based loading setup for structural analysis.

4.2. Experimental characterization methods

4.2.1. Measurement of fiber orientation

The fiber orientation data is experimentally measured by CT volumetric image of the demonstrator using an Yxlon X-ray CT system with a PerkinElmer detector and a reflection tube by Comet. In order to ensure a suitable resolution, the demonstrator is cut into four equal parts along the longitudinal and transverse axis using a band saw and the two quarters without hole are scanned. The detector has a resolution of 2048 × 2048 pixels and a pixel pitch of 200 µm. A final 16-bit volumetric gray value voxel image is reconstructed from the projection data using the Feldkamp, Davis and Kress (FDK) algorithm [66]. Since the geometry of the demonstrator (except of the machined hole) is symmetric to one axis (see Fig. 5), the two volumetric images of the quarters have been merged and flipped in order to gain one overall volumetric voxel image of the whole demonstrator. The resolution of the resulting data is 67.3 µm per voxel. The fiber orientation in each voxel of the reconstructed volume is determined using the algorithm presented in Section 3.3.2. In order to define fiber and matrix material, a threshold is set by hand in a way that fiber rovings are clearly visible. Voxels with gray values higher than this threshold are considered fiber material and taken into account for the statistical description of the fiber orientation. The fiber orientation in each voxel of the reconstructed volume was determined using an algorithm based on the structure tensor as described by Pinter et al. [53].

4.2.2. Cyclic four-point bending tests

A four-point bending test with cyclic loading arrangement is performed on a Zwick Roell universal testing machine with 500 kN load

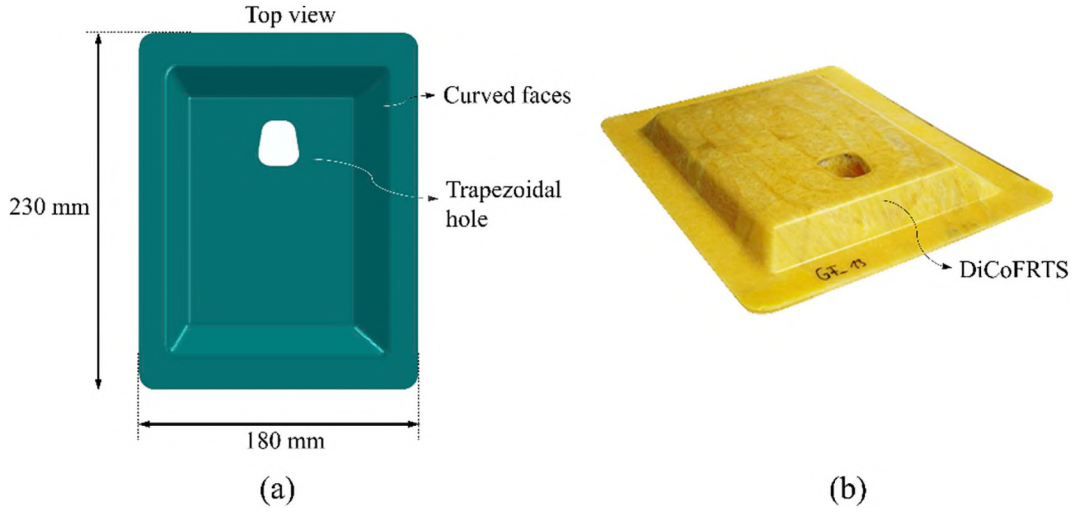

Fig. 5. (a) Geometrical model of demonstrator, (b) physical model of SMC demonstrator.

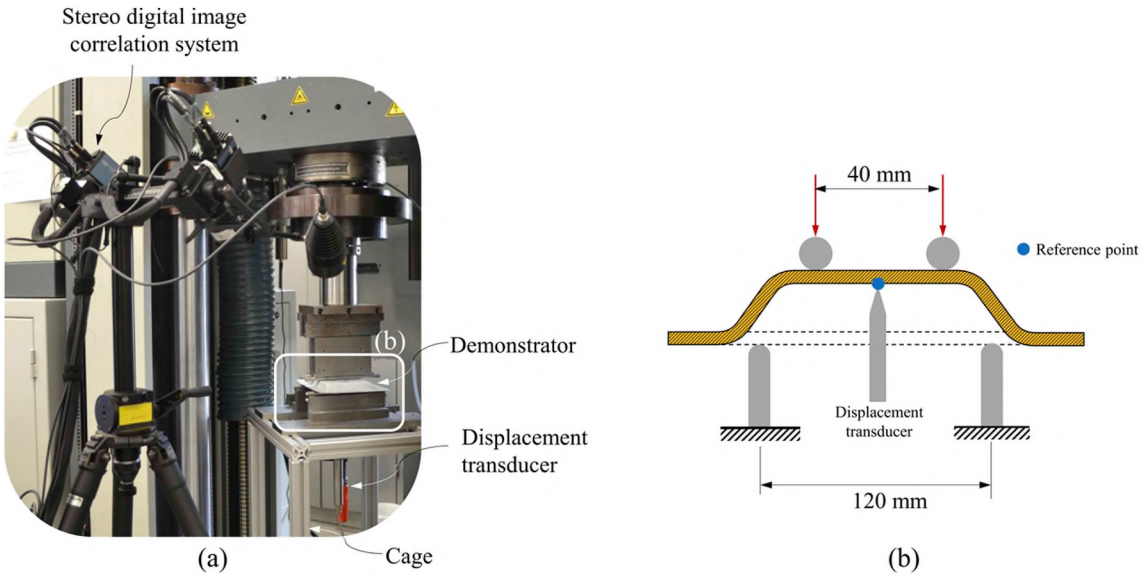

Fig. 6. (a) Experimental configuration of the four-point bending test with stereo DIC, (b) schematic close up of the four-point bending setup.

capacity (Fig. 6). The specimen is placed on two lower supports, which are aligned at a distance of 120 mm. The supports themselves are mounted on a cage to be able to measure the local deflection directly below the reference center point of the demonstrator with a tactile transducer.

The demonstrator is loaded by two cylindrical indenters with 10 mm diameter, having a distance of 40 mm. The displacement field of the demonstrator is measured with a stereo digital image correlation (DIC) system (GOM 4 M). After reaching a preload of 100 N, to ensure contact between the demonstrator and the upper supports, the DIC system captures images with a frame rate of 1 Hz up to final fracture. The four-point bending test is then carried out cyclically with a constant nominal crosshead speed of 2 mm/min. Each loading sequence consists of a first maximum deflection, which increases from 0.5 mm to 5 mm and four subsequent sub-cycles in the range of 30%–70% of the preceded maximum deflection value. Between different loading sequences, a load of 100 N is maintained for 90 s. After eight loading sequences, the deflection is increased until fracture of the demonstrator (Fig. 7).

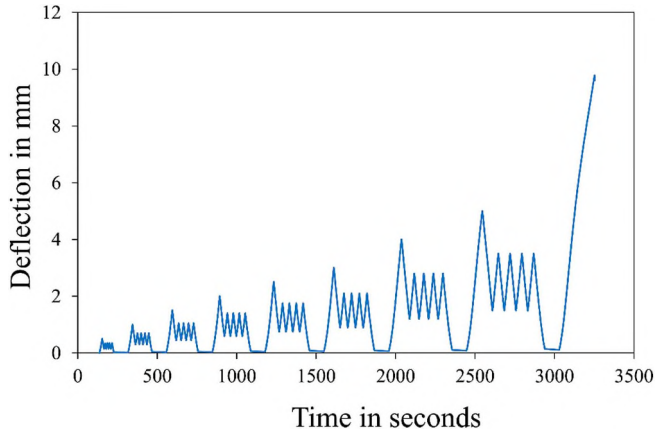

Fig. 7. Loading-unloading sequence of cyclic four-point bending tests.

4.2.3. *Measurement of friction coefficient*

The friction coefficient between the indenters and the demonstrator is measured (Fig. 8) with respect to DIN EN ISO 8295. Cylindrical pins used as indenters in the four-point bending experiments are joined to a flat metal sheet for placement of loads and they are used as a slider. A wire is redirected by a ball bearing mounted sheave and connected to the 50 N load cell of a Zwick 2.5 kN universal testing machine. The other side of the wire pulls the slider loaded with additional weights over the clamped SMC plate for a total length of 70 mm. The total weight force is 52 N and the testing speed is 100 mm/min. Before testing, both the cylindrical pins and the SMC plate are cleaned using isopropyl alcohol. For evaluation of the data, the average value of the force between the slider's position at 10 mm and 60 mm is considered. This test is repeated seven times leading to a friction coefficient of 0.24 ± 0.01. Further investigations indicate that the friction coefficient is independent of different weights and testing speeds.

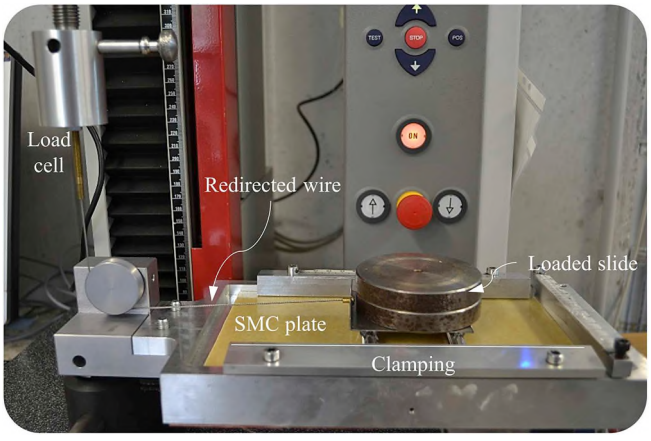

Fig. 8. Experimental setup for measuring the friction coefficient between SMC plate and steel.

4.3. *Simulation*

4.3.1. *Overview*

The key steps of the implemented models and their corresponding sequence are shown in the flow chart in Fig. 9. Compression molding

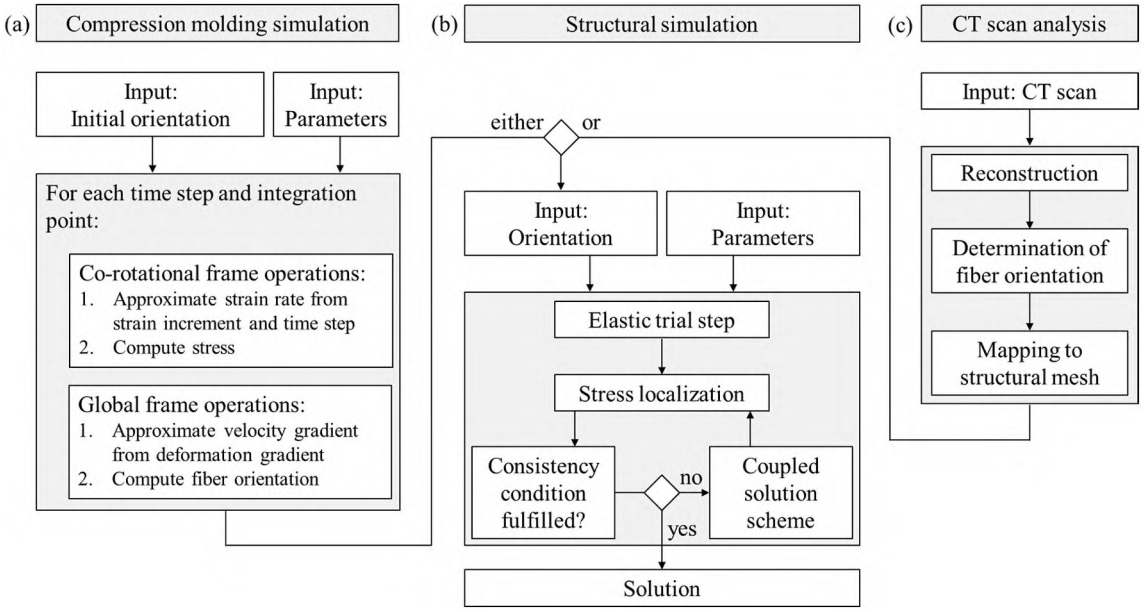

Fig. 9. Flow chart describing the key steps of the modeling approaches presented in Section 3, (a) compression molding simulation, (b) structural simulation, (c) CT scan analysis.

simulation starts with the input of an initial fiber orientation and material parameters. For each time step and integration point the strain rate, stress, deformation gradient and fiber orientation are computed. The final orientation information serves as input for the structural simulation. Here, the stress in each integration point is calculated. Based on the consistency condition, damage is computed via a coupled solution scheme until convergence. An alternative input for the fiber orientation is provided by the CT scan analysis. Hereby, the part is scanned and subsequently virtually reconstructed. The fiber orientation is determined and mapped onto the structural mesh.

4.3.2. *Compression molding simulation*

The molding of SMC consists of two steps, a forming step and consecutive flow of the material. First, the planar stack of cut sheets is preformed manually in the lower mold, which is reflected as a deformation of the stack by the upper mold in this simulation (compare Fig. 10(a) and (b)). It is assumed that fibers are randomly oriented in plane with no fibers oriented normal to the stack initially, as it is built from planar sheets. The forming does not involve a significant amount of flow and utilizes a Lagrangian mesh for accurate yet computationally inexpensive results. Flow starts as soon as the mold gap equals the thickness of the initial charge and the Lagrangian mesh would deform excessively. In view of this, the preformed material distribution and fiber orientation state are mapped to an Eulerian mesh within a Coupled-Eulerian-Lagrangian (CEL) method to simulate SMC flow through the mesh instead of a deformation with the mesh. The Eulerian domain covers the entire molding volume and extends a few element layers beyond each mold (compare Fig. 3(b)), resulting in 220,000 hexahedrons in total. The average element size is 5 mm in plane and 1 mm in thickness and stays fixed during the simulation (no moving mesh and no adaptivity are applied). All four side boundaries of the mold (colored pink in Fig. 10) restrict the flow to have no velocity component in normal direction, thus representing the side-walls of the mold allowing for no leakage. The molds itself are considered stiff and are modeled as rigid body shells. A contact definition prevents penetration of the molds.

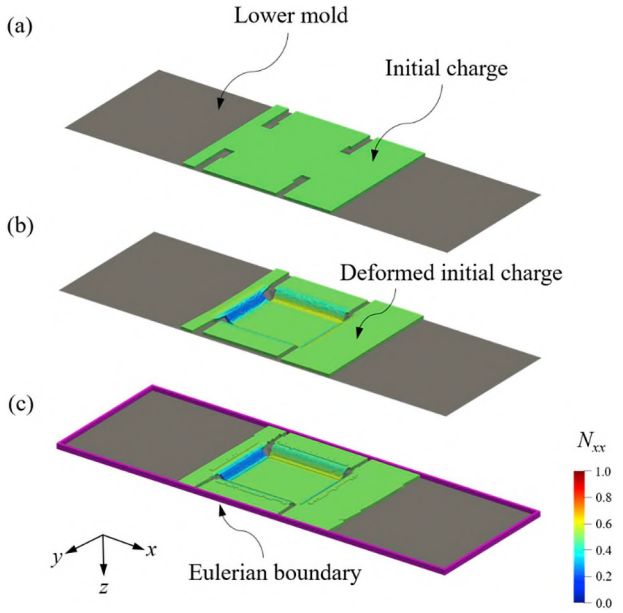

Fig. 10. Generation of the initial fiber orientation state for the compression molding simulation indicating N_{xx}, (a) the initial charge is modeled as Lagrangian body and is placed in the lower mold, (b) the charge is deformed by the upper mold (not shown here) until the gap equals the stack thickness, (c) the initial state is mapped to a Eulerian mesh for the compression molding simulation.

Equations (6)–(10) are implemented using a VUMAT subroutine utilizing six state variables to describe the components of the orientation tensor. While the computation of stresses is based on the strain rate computed in the co-rotational framework, the change of fiber orientation is computed based on the velocity gradient according to Equation (5). The subroutine has been carefully validated with simple finite strains and rigid body rotations.

4.3.3. *Structural simulation of damage*

Cyclic four-point bending simulations are performed to investigate

the structural behavior of the demonstrator using ABAQUS. The demonstrator is meshed using about 30,000 four-node S4 shell elements. The indenters used in the experimental setup (Fig. 6) are modeled as rigid. In order to adequately capture the actual behavior, the two lower indenters are fixed and the two upper indenters are displaced cyclically in a vertical fashion. The friction coefficient between the indenters and the demonstrator is determined experimentally (see Section 4.2.3). The elastic fiber properties and the matrix behavior of pure UPPH are available in Table A.2. The interface strength distribution parameters for the UPPH glass fiber system (used in the demonstrator) are taken from Refs. [39,56].

5. Results and discussion

5.1. Validation of the compression molding simulation

Fig. 11 illustrates the deformed shape during molding. The initial charge is compacted in the beginning and the cutouts, which are designed for improved forming, are filled with SMC material. As soon as the SMC mass forms a uniform chunk of material, significant extensional flow in both directions of the cavity starts. It can be observed that the side with a slightly longer flow path (pointing downwards in Fig. 11) and larger initial mold coverage experiences a uniform velocity at the flow front leading to a linear front. The side with a shorter overall flow path (pointing upwards in Fig. 11) shows a slightly V-shaped flow front arising from the fact that material from the flanks flows faster than the material of the central area that has a longer, curved path.

The second order fiber orientation tensor resulting from the compression molding simulation is mapped to the shell mesh of the machined demonstrator and compared to the results obtained with CT analysis. Furthermore, another compression molding simulation is performed with a commercial mold filling software, and these results are also compared to the CT analysis results and to the results of the model presented here. The upper two rows of Fig. 12 show the CT scans

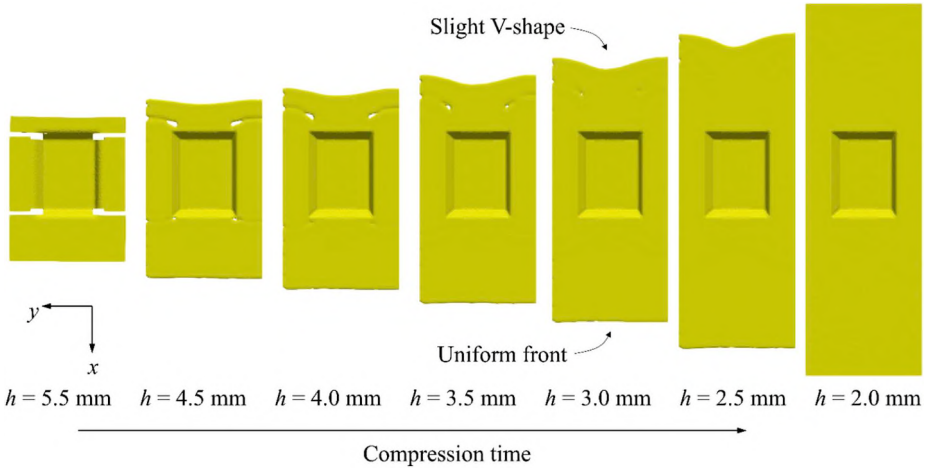

Fig. 11. Flow front positions at different mold gaps h. The overall tool size is 800 mm × 250 mm.

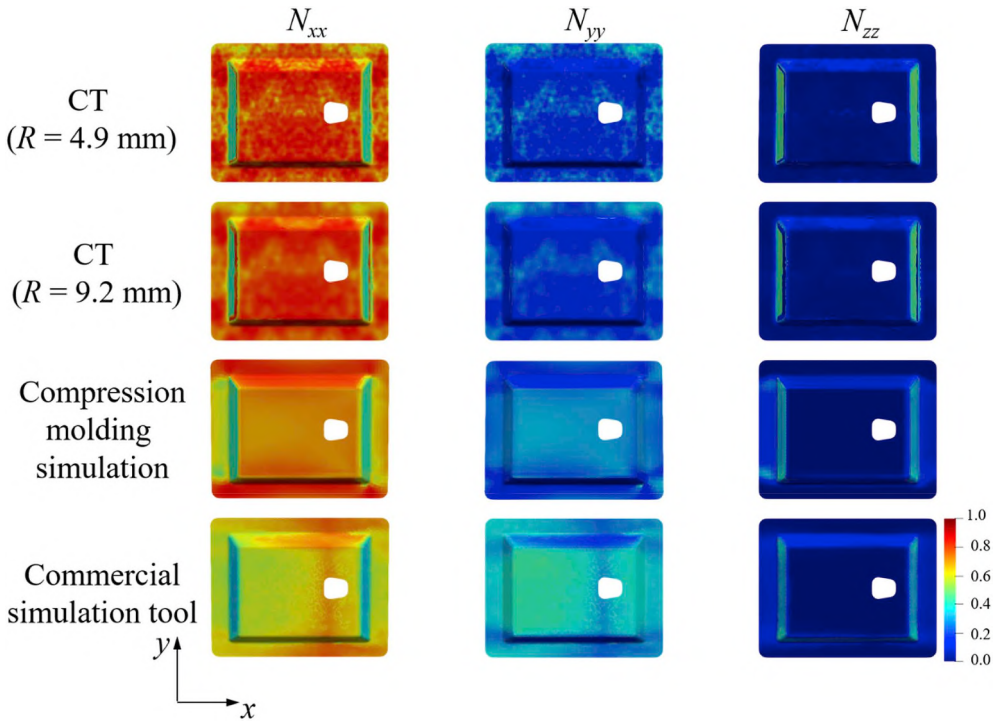

Fig. 12. Comparison of fiber orientation tensors obtained from compression molding simulations as well as CT scans. Two different evaluation radii R are used to obtain fiber orientation tensors from the CT scan, and are compared to the compression molding simulation described in Section 4.3.2 as well as a result from a commercial simulation tool. The simulation results are mapped to the machined demonstrator including the trapezoidal hole.

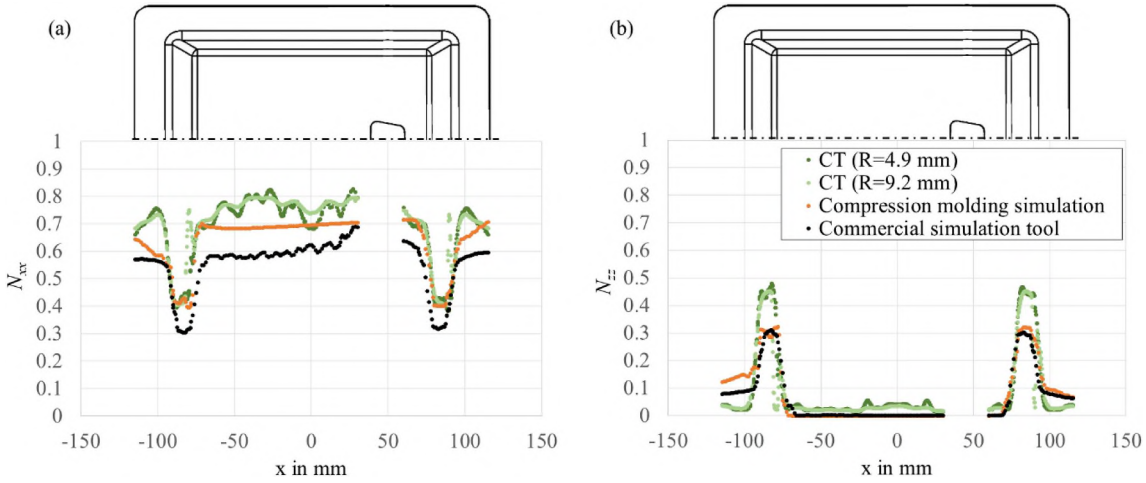

Fig. 13. Fiber orientation tensor components along the cross section for $y \equiv 0$, (a) component N_{xx}, (b) component N_{zz}.

with the two evaluation radii $R = 4.9$ mm and $R = 9.2$ mm, whereas the following two rows result from the compression molding simulation described in Section 4.3.2 and from a commercial software tool. This illustration is supplemented with Fig. 13 to quantitatively evaluate the N_{xx} and N_{zz} components of the second order fiber orientation tensor at the section of plane $y = 0$ (see also plane B in Appendix A.1). The N_{yy} component is omitted, as it is redundant ($\mathrm{tr}(\boldsymbol{N}) = 1$). It has to be noted that the simulation results describe fiber orientations in a statistical sense, while it is compared to a CT scan representing one random realization of a statistical process.

All results show a significant fiber alignment in the extensional flow direction - with local variations in the CT scan and a smooth result of the simulation. The N_{xx} component shows an almost unidirectional alignment of fibers along the scanned part, whereas the compression molding simulation computes a slightly lower degree of orientation or significantly lower degree of orientation in case of the commercial tool. The computed N_{xx} component of the compression molding simulation agrees well with CT scan data, especially in the sloped regions. Consequently, both simulations show a higher degree of orientation in the perpendicular direction (N_{yy}). The N_{zz} component is only pronounced in the sloped flanks of the demonstrator indicating a vanishing component normal to the shell direction. This is expected and supports the use of Equation (10), since an explicit diffusion coefficient would increase fiber orientation values in N_{zz} .

The difference in N_{xx} direction between CT scans and simulations can be attributed partly to the averaging nature of the simulation compared to a single scanned demonstrator which explains local features in the scans that are not visible in the simulation results.

5.2. Validation of the structural simulation

Results gained from the structural simulations are compared and validated with experimental observations by means of the force-displacement relation of a reference point and full-field strain measurements. For the former, the reference point is defined in the center of the simulated demonstrator analogously to the experimental set-up (see Section 4.2.2). The applied force is measured at the upper supports of

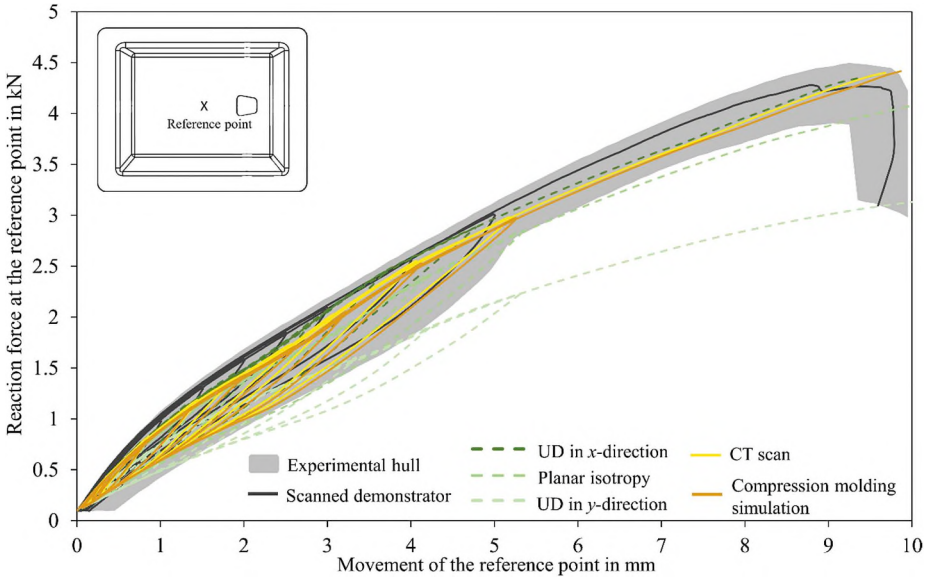

Fig. 14. Comparison of force-displacement curves of the demonstrator reference point. Gray: experimentally measured curves. Dashed green: results coming from artificial initial fiber orientation states. Solid yellow and solid orange: results coming from measured and simulated initial fiber orientation states. (For interpretation of the references to color in this figure legend, the reader is referred to the Web version of this article.)

the modeled testing device. Fig. 14 compares experimentally measured force-displacement curves with various force-displacement curves for the reference point obtained from simulations with different initial fiber orientation distributions. All other simulation boundary conditions and material parameters remain consistent. In a first simulation, the initial fiber orientation is assumed to be planar isotropic, as the used SMC sheets are approximately planar isotropic. Besides, initially unidirectional orientations in x-direction and y-direction are used as input for reference purposes. Furthermore, simulations using the measured fiber orientation state of the scanned demonstrator as input are performed (see Section 3.3.2), as well as simulations with input coming from the molding simulation of the virtual process chain (see Section 3.3.1).

The experimentally measured force-displacement curves of the investigated demonstrators show a similar behavior with a relatively low scatter. In Fig. 14 the force-displacement curve of the scanned demonstrator is shown in dark gray and the corresponding scatter on basis of the remainder of the measured experiments is shown as a light gray area. The eight successively applied loading cycles form eight hystereses before in the ninth cycle the demonstrator is loaded until failure. The hystereses most likely have their origin in the dissipated energy due to friction between indenters and demonstrator. The predicted behavior of the considered reference point depends on the initial fiber orientation state considered from the aforementioned SMC sheet assumptions, CT scans and molding simulations. From the green, dashed curves, it can clearly be seen that a unidirectional fiber placement in y-direction leads to the softest response, as the reinforcements are perpendicular to the bending load. In contrast to that, unidirectional fibers in x-direction lead to the stiffest response. The force-displacement curve obtained from an initially planar isotropic fiber orientation state lies in between. The yellow and orange, solid curves show that both, the responses due to the measured fiber orientation and the responses due to the simulated orientations of the virtual process chain, behave similar. Despite the fact that the initial orientation of the SMC sheets is more or less planar isotropic, the force-displacement curves of the final demonstrator are more akin to the force-displacement curve of the unidirectional orientation in x-direction. This agrees with the observations from the compression molding simulation as shown in Section 5.1.

In addition to the measured reference point, full-field strain measurements are performed and compared to the simulation results. As the demonstrator is rather brittle, the principal strain ε_1 is considered an appropriate variable for full-field measurement. This is also covered by the corresponding structural damage model as presented in Section 3.4. The DIC image in Fig. 15(a) suggests that the main load path, connecting the upper and lower indenters, is aligned with the sloped flanks of the structure. In this area, the compression molding simulation shows highest accuracy compared to the CT scanned part (see Figs. 12 and 13). This is therefore directly related to the overall accuracy of the force-displacement curve shown in Fig. 14. The planar region of the demonstrator plays a minor role for the load transfer. The calculation of the damage evolution corresponds to the experimental observations. Interface and matrix damage are highest in areas which bear the highest loadings, as can be seen in Fig. 15(c). Here, the fiber volume fraction $\bar{c}_F$ of load-carrying fibers with intact interfaces is shown. The red colored regions are sound with a load-carrying fiber volume fraction of about 25%. The green colored regions indicate that fiber-matrix interfaces are destroyed and therefore the load-carrying fiber volume fraction $\bar{c}_F$ is decimated. These critical areas are identified correctly by the model calculations. The matrix is damaged approximately 20% in these critical areas. All experiments show a macroscopic crack initiation in one of the highly loaded and damaged areas, as can be seen in Fig. 15(b). The exact point of macroscopic crack initiation depends on various (statistically random) influence factors and is not captured within the implemented damage model.

In Fig. 16 a comparison of the simulated fractions of load-carrying fibers $\bar{c}_F$ within the demonstrator shortly before failure is shown. Fig. 16(a) shows the calculated result for a fiber orientation state that is initially UD in x-direction. The most damaged areas are the corners and the lower edge with the steeper slope. Fig. 16(c) shows that, for a fiber orientation which initially is UD in y-direction, the most damaged areas are the ones between the two upper indenters. An initially planar isotropic fiber orientation leads to a combination of the two described UD cases. The damage is spread wider over the demonstrator, but is also attenuated, as can be seen in Fig. 16(b). The results obtained for the case of the measured CT scan and the simulated fiber orientation state are shown in Fig. 16(d) and (e). Hereby, it can be clearly observed that the plots vary between the results coming from UD in x-direction and an initially planar isotropic state. This is in good agreement with the observed and simulated fiber orientation state after the compression molding process.

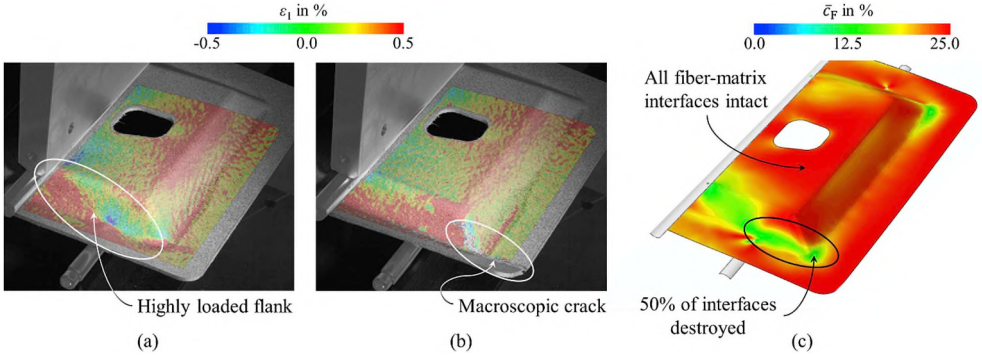

Fig. 15. (a) Measured maximum principal strain field ε_1 showing highly loaded flank of the demonstrator before failure, (b) macroscopic area of failure, (c) corresponding simulated interface damage showing the volume fraction $\bar{c}_F$ of fibers with intact interfaces slightly before failure.

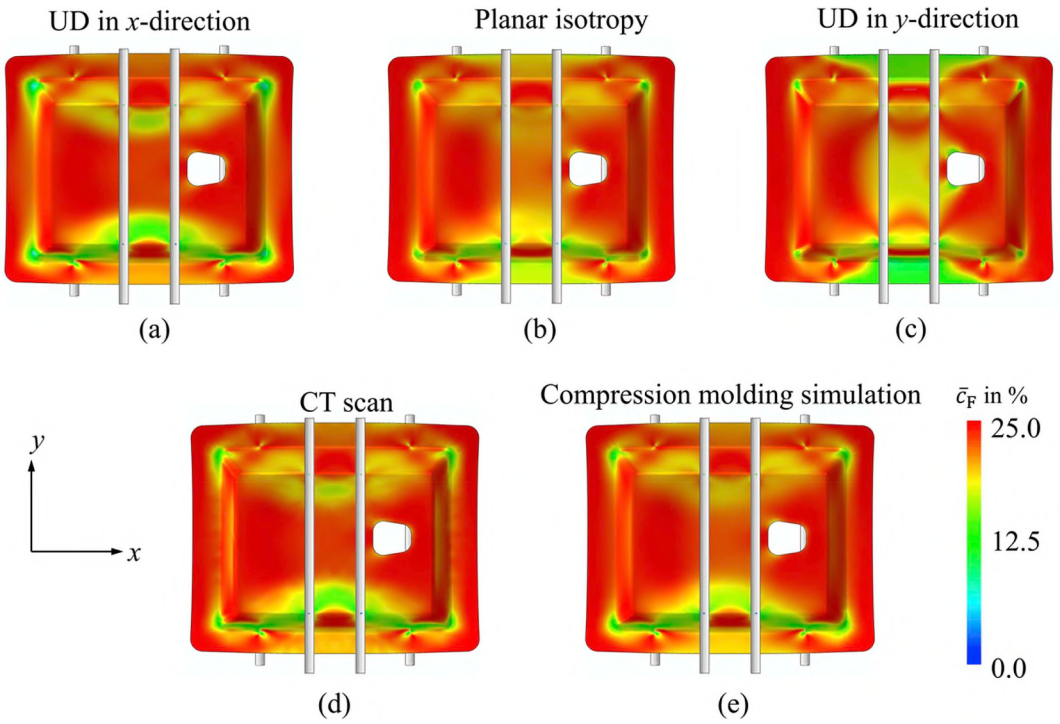

Fig. 16. Comparison of the fraction $\bar{c}_F$ of load-carrying fibers with intact interfaces for different initial fiber orientations, shortly before macroscopic failure. Red areas are fully intact with a load-carrying fiber volume fraction of about 25%. In green areas, half of the fiber-matrix interfaces and 20% of the matrix are destroyed. (For interpretation of the references to color in this figure legend, the reader is referred to the Web version of this article.)

6. Conclusions

A virtual process chain for SMC including the key simulation steps, i.e. compression molding and structural simulation with an interface for data transfer among the steps, is established successfully for any SMC composite part. A demonstrator fabricated through the physical process chain is used for experimental validations of the virtual process chain.

CT scans of the demonstrator show high re-orientations induced by flow and indicate the need to take these re-orientations into account. However, CT scans are not applicable during virtual product development and impractical at industrial scales. Therefore, compression simulation is necessary. Currently, commercial mold filling tools are not able to accurately predict the SMC specific plug flow. The 3D compression molding model, which takes anisotropic non-Newtonian viscosity, friction boundary conditions of the “plug-flow” and Jeffery's evolution equation for fiber orientations into account, leads to improved predictions.

A neutral VTK data format is used to establish a seamless mapping of fiber orientation from compression molding simulation to structural simulation. Further, a distance-based weighting method is developed to map the second order orientation tensor from a CT scan to the Gaussian points of a finite element mesh. These mapping procedures enable to account for the spatially varying high anisotropy of the material in the structural simulation.

Using mapped orientation data from the compression molding simulation, the structural simulation of the performed four-point bending tests show that the overall mechanical behavior of the demonstrator can be reproduced accurately. Furthermore, the critical points of high damage concentrations leading to failure are predicted reliably and correctly. Structural simulations based on the fiber orientation data provided by CT scans lead to comparable results to the data from the compression molding simulation. Therefore, utilization of the presented virtual process chain can reduce costly and time-consuming CT scan procedures. The product development process is accelerated by accounting for manufacturing effects, even before physical prototypes are produced.

In future research, the virtual process chain can be used for a closed optimization loop to optimize the manufacturing process with a reduced amount of experiments during the setup of a new production line. The virtual process chain can be extended by transferring variable fiber volume fractions and accounting for machining processes after molding. Residual stresses due to curing can be incorporated to improve the simulation of structural performance. An accurate prediction of curing state may enable earlier demolding and handling, and thus reduce the cycle time in a continuous production process of SMC. Further, mesoscopic modeling of fiber bundles can improve compression molding simulations of SMC by eliminating the need for closure approximations and enabling fiber separation effects, especially at complex geometrical features, such as ribs.

Contributions

JG, MS and TB developed and implemented the structural damage model. NM and MH developed and implemented the compression molding simulation. LS and PP performed CT analysis and developed the method to map measured fiber orientations. AT carried out four-point bending tests including DIC measurements. PP measured the friction coefficient between SMC and the steel indenters. JG, NM and TDP gathered all the individual contributions to the process chain and combined these to the manuscript with initial support from MS and MH. LK, TB and TS supervised the method developments and supported the discussion of simulation results. PE, AH and FH supervised the work in terms of composite process knowledge and relevance of the addressed subjects. KW supervised the microstructural and mechanical investigations and supported the discussion of experimental characterization results.

Acknowledgements

The research documented in this paper has been funded by the German Research Foundation (DFG) within the International Research Training Group “Integrated engineering of continuous-discontinuous long fiber reinforced polymer structures” (GRK 2078). The support by the German Research Foundation (DFG) is gratefully acknowledged. The authors also gratefully acknowledge Fraunhofer Institute of Chemical Technology for fabrication of the demonstrator by compression molding process. The authors gratefully acknowledge the support of licenses for MapLib by Fraunhofer Institute for Algorithms and Scientific Computing.

Appendix

A.1 Dimensional Details of the Demonstrator.

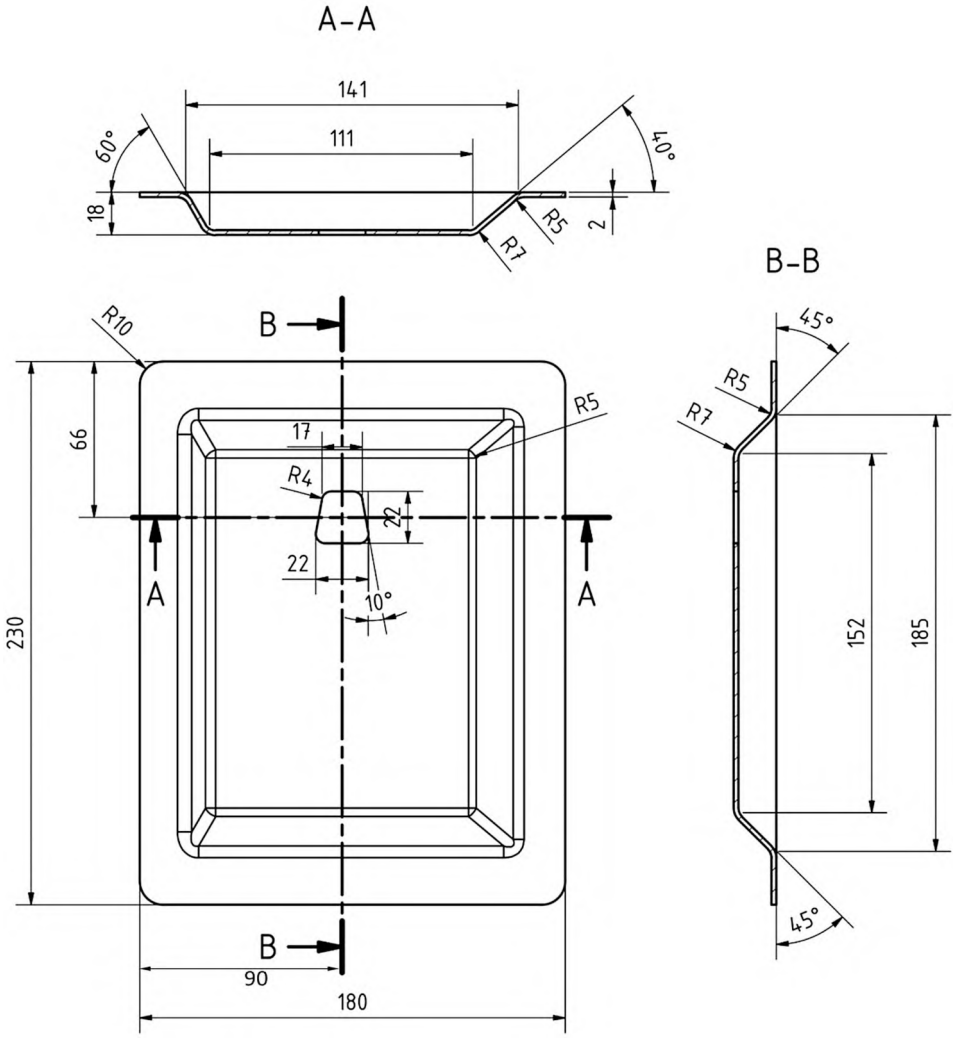

Fig. A.1. Dimensions of the demonstrator.

A.2 Material Data.

Table A.2
Material parameters.

Parameter	Symbol	Value	Unit
Compound properties			
Fiber volume fraction	c_F	0.25	–
Fiber diameter	d_F	13.5	µm
Fiber length	l_F	25.4	mm
Compound mass density	ρ_0	1900	kg/m^3
Mechanical properties used in structural simulation			
Initial Matrix Young's Modulus	E_M^0	3.06	GPa
Initial Matrix Poisson's Ratio	ν_M^0	0.3	–
Fiber Young's Modulus	E_F	73	GPa

(*continued on next page*)

Table A.2 (*continued*)

Parameter	Symbol	Value	Unit
Fiber Poisson's Ratio	ν_F	0.22	–
Interface parameter	σ_u	4.5	MPa
Interface parameter	$\frac{1}{(A_{I0})^{1/k}}\frac{1}{\sigma_0}\hat{\sigma}_{I,eq}$	87.5004	$1/m^2$
Interface parameter	k	1.5017	–
Mechanical properties used in compression molding simulation			
Speed of sound in compound	ζ_0	400	m/s
Reference viscosity	η_0	0.4	MPa s
Reference strain rate	D_0	1	1/s
Power-Law coefficient	n	0.44	–
Anisotropic coupling term	α	10	–
Friction stress	κ	30000	Pa

References

[1] Bruderick M, Denton D, Shinedling M, Kiesel M. Applications of carbon fiber SMC for the dodge viper. Proc. Second S.P.E. Automot. Compos. Conf. Exhib. 2002;1:1–10.

[2] Gardinger G. Is the BMW 7 Series the future of autocomposites? Composites World. 2016https://www.compositesworld.com/articles/is-the-bmw-7-series-the-future-of-autocomposites.

[3] Wilkinson AN, Ryan AJ. Polymer procesing and structure development. *Springer Netherlands*; 1998.

[4] Afazov SM, Becker AA, Hyde TH. Development of a finite element data exchange system for chain simulation of manufacturing processes. Adv Eng Software May 2012;47(1):104–13.

[5] Spiess H, Oeckerath A, Landvogt B. Mapping library manual. 2010Version 2010.1.

[6] Wolf K, Bayrasy P, Brodbeck C, Kalmykov I, Oeckerath A, Wirth N. MpCCI: neutral interfaces for multiphysics simulations. In: Griebel M, Schüller A, Schweitzer MA, editors. In *scientific Computing and Algorithms in industrial simulations*. Cham: Springer International Publishing; 2017. p. 135–51.

[7] Reclusado CA, Nagasawa S. Modeling of fiber-reinforced plastics taking into account the manufacturing process. Institute of structural analysis and antiseismic research school of civil engineering national technical university of athens. 2016. p. 2220–35.

[8] Kärger L, Bernath A, Fritz F, Galkin S, Magagnato D, Oeckerath A, Schön A, Henning F. Development and validation of a CAE chain for unidirectional fibre reinforced composite components. Compos Struct Nov. 2015;132:350–8.

[9] Mayer N, Van Den Broucke B, Prowe J, Havar T, Hinterhölzl R. Finite element mapping for incompatible FE meshes of composite structures. Adv Eng Software Sep. 2016;99:81–8.

[10] Kärger L, Galkin S, Zimmerling C, Dörr D, Linden J, Oeckerath A, et al. Forming optimisation embedded in a CAE chain to assess and enhance the structural performance of composite components. Compos Struct May 2018;192:143–52.

[11] Buck F, Brylka B, Müller V, Müller T, Weidenmann KA, Hrymak AN, Henning F, Böhlke T. Two-scale structural mechanical modeling of long fiber reinforced thermoplastics. Compos Sci Technol 2015;117:159–67.

[12] Hohberg M, Kärger L, Hrymak A, Henning F. Process simulation of sheet molding compound (SMC) as key for the integrated simulation chain. NAFEMS Seminar: “Simulation von Composites – Bereit für Industrie 4.0? 2016. p. 3.

[13] Orgéas L, Idris Z, Geindreau C, Bloch JF, Auriault JL. Modelling the flow of power-law fluids through anisotropic porous media at low-pore Reynolds number. Chem Eng Sci Jul. 2006;61(14):4490–502.

[14] Perez-Miguel M, Abisset-Chavanne E, Chinesta F, Keunings R. From dilute to entangled fiber suspensions involved in reinforced polymers and composites. AIP conference proceedings, vol. 1896. 2017:030006. 1.

[15] Fan X, Phan-Thien N, Zheng R. A direct simulation of fibre suspensions. J. Nonnewton. Fluid Mech. Jan. 1998;74(1–3):113–35.

[16] Kuhn C, Walter I, Täger O, Osswald T. Simulative prediction of fiber-matrix separation in rib filling during compression molding using a direct fiber simulation. J. Compos. Sci. Dec. 2017;2(1):2.

[17] Hayashi S, Chen H, Hu W. 5 th international LS-DYNA ® users conference development of new simulation Technology for compression molding of long fiber reinforced plastics using LS-DYNA ®. 5 th international LS-DYNA ® users conference development of new simulation Technology for compression molding of long fiber reinforced plastics using LS-DYNA ®. 2018.

[18] Silva-Nieto RJ, Fisher BC, Birley AW. Predicting mold flow for unsaturated polyester resin sheet molding compounds. Polym Compos Sep. 1980;1(1):14–23.

[19] Castro JM, Griffith RM. Sheet molding compound compression-molding flow. Polym Eng Sci May 1989;29(10):632–8.

[20] Barone MR, Caulk DA. A model for the flow of a chopped fiber reinforced polymer compound in compression molding. J Appl Mech 1986;53(2):361.

[21] Barone MR, Osswald TA. A boundary element analysis of flow in sheet molding compound. Polym Compos Apr. 1988;9(2):158–64.

[22] Liang EW, T. I CL. A finite element method for flow in compression molding of thin and thick parts. Polym Compos 1995;16(1):70–82.

[23] Abrams LM, Castro JM. Predicting molding forces during sheet molding compound (SMC) compression molding. I: model development. Polym Compos Jun. 2003;24(3):291–303.

[24] Dumont P, Orgéas L, Favier D, Pizette P, Venet C. Compression moulding of SMC: in situ experiments, modelling and simulation. Compos. Part A Appl Sci Manuf Feb. 2007;38(2):353–68.

[25] Guiraud O, Dumont PJJ, Orgéas L, Favier D. Rheometry of compression moulded fibre-reinforced polymer composites: Rheology, compressibility, and friction forces with mould surfaces. Compos. Part A Appl Sci Manuf Nov. 2012;43(11):2107–19.

[26] Hohberg M, Kärger L, Bücheler D, Henning F. Rheological in-mold measurements and characterizations of sheet-molding-compound (SMC) Formulations with different constitution properties by using a compressible shell model. Int Polym Process Nov. 2017;32(5):659–68.

[27] Kehrer L, Wicht D, Wood JT, Böhlke T. Dynamic mechanical analysis of pure and fiber-reinforced thermoset- and thermoplastic-based polymers and free volume-based viscoelastic modeling. GAMM-Mitteilungen Apr. 2018;41(1):e201800007.

[28] Schemmann M, Lang J, Helfrich A, Seelig T, Böhlke T. Cruciform specimen design for biaxial tensile testing of SMC. J. Compos. Sci. Mar. 2018;2(1):12.

[29] Fitoussi J, Bourgeois N, Guo G, Baptiste D. Prediction of the anisotropic damaged behavior of composite materials: introduction of multilocal failure criteria in a micro-macro relationship. Comput Mater Sci Feb. 1996;5(1–3):87–100.

[30] Mura T, Cheng PC. The elastic field outside an ellipsoidal inclusion. J Appl Mech 1977;44(4):591–4.

[31] Mura T. Micromechanics of defects in solids. Second Re Dodrecht, Boston, Lancaster: Martinus Nijhoff Publishers; 1987.

[32] Fitoussi J, Guo G, Baptiste D. Determination of a tridimensional failure criterion at the fibre/matrix interface of an organic-matrix/discontinuous-reinforcement composite. Compos Sci Technol Jan. 1996;56(7):755–60.

[33] Fitoussi J, Guo G, Baptiste D. A statistical micromechanical model of anisotropic damage for S.M.C. composites. Compos Sci Technol 1998;58(5):759–63.

[34] Desrumaux F, Meraghni F, Benzeggagh ML. Micromechanical modelling coupled to a Reliability approach for damage evolution prediction in composite materials. Appl Compos Mater 2000;7(4):231–50.

[35] Meraghni F, Blakeman CJ, Benzeggagh ML. Effect of interfacial decohesion on stiffness reduction in a random discontinuous-fibre composite containing matrix microcracks. Compos Sci Technol 1996;56(5):541–55.

[36] Desrumaux F, Meraghni F, Benzeggagh ML. Generalised Mori-Tanaka scheme to model anisotropic damage using numerical Eshelby tensor. J Compos Mater 2001;35(7):603–24.

[37] Ju JW, Lee HK. A micromechanical damage model for effective elastoplastic behavior of ductile matrix composites considering evolutionary complete particle debonding. Comput Methods Appl Mech Eng Mar. 2000;183(3–4):201–22.

[38] Zaïri F, Naït-Abdelaziz M, Gloaguen JM, Bouaziz A, Lefebvre JM. Micromechanical modelling and simulation of chopped random fiber reinforced polymer composites with progressive debonding damage. Int J Solids Struct Oct. 2008;45(20):5220–36.

[39] Schemmann M, Görthofer J, Seelig T, Hrymak A, Böhlke T. Anisotropic meanfield modeling of debonding and matrix damage in SMC composites. Compos Sci Technol Jun. 2018;161:143–58.

[40] Müller V, Böhlke T. Prediction of effective elastic properties of fiber reinforced composites using fiber orientation tensors. Compos Sci Technol Jun. 2016;130:36–45.

[41] Advani SG, Tucker III CL. The use of tensors to describe and predict fiber orientation in short fiber composites. J Rheol (N Y N Y) 1987;31(8):751–84.

[42] Kanatani K-I. Distribution of directional data and fabric tensors. Int J Eng Sci Jan. 1984;22(2):149–64.

[43] Barone MR, Caulk DA. The effect of deformation and thermoset cure on heat conduction in a chopped-fiber reinforced polyester during compression molding. Int J Heat Mass Transf Jul. 1979;22(7):1021–32.

[44] Hohberg M. Experimental investigation and process simulation of the compression molding process of Sheet Molding Compound (SMC) with local reinforcements. ” To be Publ.; 2019.

[45] Benson DJ. “Computational methods in Lagrangian and Eulerian hydrocodes,” *comput*. Methods Appl. Mech. Eng. Sep. 1992;99(2–3):235–394.

[46] Benson DJ, Okazawa S. “Contact in a multi-material Eulerian finite element formulation,” *Comput*. Methods Appl. Mech. Eng. Oct. 2004;193(39–41):4277–98.

[47] Hohberg M, Kärger L, Henning F, Hrymak A. Rheological measurements and

rheological shell model considering the compressible behavior of long fiber reinforced sheet molding compound (SMC). Compos. Part A Appl Sci Manuf Apr. 2017;95:110–7.
[48] Latz A, Strautins U, Niedziela D. Comparative numerical study of two concentrated fiber suspension models. J. Nonnewton. Fluid Mech. Jul. 2010;165(13–14):764–81.
[49] Chung DH, Kwon TH. Invariant-based optimal fitting closure approximation for the numerical prediction of flow-induced fiber orientation. J Rheol (N Y N Y) Jan. 2002;46(1):169–94.
[50] Phelps JH, Tucker CL. An anisotropic rotary diffusion model for fiber orientation in short- and long-fiber thermoplastics. J. Nonnewton. Fluid Mech. Feb. 2009;156(3):165–76.
[51] Sommer DE, Favaloro AJ, Pipes RB. Coupling anisotropic viscosity and fiber orientation in applications to squeeze flow. J Rheol (N Y N Y) May 2018;62(3):669–79.
[52] Jeffery GB. The motion of ellipsoidal particles immersed in a viscous fluid. Proc. R. Soc. A Math. Phys. Eng. Sci. Nov. 1922;102(715):161–79.
[53] Pinter P, Dietrich S, Bertram B, Kehrer L, Elsner P, Weidenmann KA. Comparison and error estimation of 3D fibre orientation analysis of computed tomography image data for fibre reinforced composites. NDT E Int Apr. 2018;95:26–35.
[54] Mori T, Tanaka K. Average stress in matrix and average elastic energy of materials with misfitting inclusions. Acta Metall May 1973;21(5):571–4.
[55] Castañeda PP, Suquet P. Nonlinear composites. Adv Appl Mech Jan. 1997;34:171–302.
[56] Görthofer J, Schemmann M, Seelig T, Hrymak A, Böhlke T. Sensitivity analysis of fiber-matrix interface parameters in an SMC composite damage model. Proceedings of the 18th international conference on experimental mechanics, vol. 2. 2018. p. 544. 8.
[57] Ogihara S, Koyanagi J. Investigation of combined stress state failure criterion for glass fiber/epoxy interface by the cruciform specimen method. Compos Sci Technol Jan. 2010;70(1):143–50.
[58] J. Koyanagi, H. Nakatani, and S. Ogihara, "Comparison of glass-epoxy interface strengths examined by cruciform specimen and single-fiber pull-out tests under combined stress state," Compos. Part A Appl Sci Manuf, vol. 43, no. 11, pp. 1819–1827, Nov. 2012.
[59] Tandon GP, Kim RY, Bechel VT. "Fiber – matrix interfacial failure charcterization using a cruciform-shaped specimen. J Compos Mater 2002;36(23):2667–91.
[60] Ben Cheikh Larbi A, Sai K, Sidhom H, Baptiste D. Constitutive model of micromechanical damage to predict reduction in stiffness of a Fatigued SMC composite. J Mater Eng Perform 2006;15(5):575–80.
[61] Crisfield MA, Moita GF. A unified co-rotational framework for solids, shells and beams. Int J Solids Struct Aug. 1996;33(20–22):2969–92.
[62] Meraghni F, Desrumaux F, Benzeggagh ML. Implementation of a constitutive micromechanical model for damage analysis in glass mat reinforced composite structures. Compos Sci Technol 2002;62(16):2087–97.
[63] Nguyen BN, Khaleel MA. A mechanistic approach to damage in short-fiber composites based on micromechanical and continuum damage mechanics descriptions. Compos Sci Technol 2004;64(5):607–17.
[64] Anagnostou D, Chatzigeorgiou G, Chemisky Y, Meraghni F. Hierarchical micromechanical modeling of the viscoelastic behavior coupled to damage in SMC and SMC-hybrid composites. Compos B Eng 2018;151:8–24. June.
[65] Hohberg M, Kärger L, Henning F, Hrymak A. Comparison of the flow and rheological behavior of two semi-structural sheet-molding-compound (SMC) based on a hybrid resin and glass or carbon fibers. 33rd annual meeting of the polymer processing society. 2017. p. 1–8.
[66] Feldkamp LA, Davis LC, Kress JW. Practical cone-beam algorithm. J Opt Soc Am A Jun. 1984;1(6):612.